

# A folded-sandwich polarization-entangled two-color photon pair source with large tuning capability for applications in hybrid quantum architectures

Otto Dietz · Chris Müller · Thomas Kreißl · Ulrike Herzog ·  
Tim Kroh · Andreas Ahlrichs · Oliver Benson

the date of receipt and acceptance should be inserted later

**Abstract** We demonstrate a two-color entangled photon pair source which can be adapted easily to a wide range of wavelengths combinations. A Fresnel rhomb as a geometrical quarter-wave plate and a versatile combination of compensation crystals are key components of the source. Entanglement of two photons at the Cs D1 line (894.3 nm) and at the telecom O-band (1313.1 nm) with a fidelity of  $F = 0.753 \pm 0.021$  is demonstrated and improvements of the setup are discussed.

**Keywords** down-conversion – non-degenerate – two-color – entangled photon source – quantum hybrid – quantum repeater

## 1 Introduction

In recent years there has been an increasing effort to realize and study quantum hybrid systems. These consist of two dissimilar systems which are in a joint quantum state. Aside from the fundamental insight gained from studying such a peculiar, perhaps multi-particle entangled state, there are also immediate applications in quantum information processing. Entanglement of a stationary and flying qubit, i.e., an electronic state with a long coherence time and a photon, respectively, represents a coherent quantum interface. Such interfaces are mandatory components of a quantum repeater [1], where entanglement has to be established between distant nodes. Experimental realizations demonstrated entanglement between a photon and a stationary state in atoms [2], ions [3], semiconductor quantum dots [4], color defect centers [5] and even superconducting qubits

[6]. A Bell measurement on two photons of each of two such states would then immediately establish entanglement between two stationary, possibly dissimilar states [7, 8].

However, an intrinsic problem of entangling two dissimilar systems via photons in such a way is that there are system-specific transitions in the individual stationary systems. At the same time, if the entanglement should be established over long distances, e.g. via optical fibers, the photons have to be in the telecom band. One possible solution of this problem is to use a pair of entangled photons of different wavelengths, which are matched to the two transitions of the stationary systems or to one transition and the telecom band (see Fig. 1).

Up to now the brightest and most practical sources of entangled photon pairs rely on spontaneous parametric down-conversion in non-linear crystals [9]. With appropriate phase-matching two-color sources with photons at different wavelengths can be realized [10, 11, 12]. For subsequent fiber coupling collinear down-conversion schemes are most convenient. Furthermore, the collinear alignment enables further integration and can be used in a monolithic design [11]. There are different possible collinear arrangements. Figure 2 shows the two-crystal Sagnac [12], the crossed-crystal [13], and the folded-sandwich configuration [14].

The rotation of the second crystal in the crossed-crystal configuration (Fig. 2 b) can be replaced by a half wave plate. Replacing the half wave plate and the second crystal by a quarter-wave plate and a mirror yields the folded-sandwich scheme (Fig. 2 c). Using only a single non-linear crystal makes it considerably easier to avoid the leakage of which-crystal information. The folded-sandwich and the crossed-crystal configuration include a compensation crystal, which compensates the

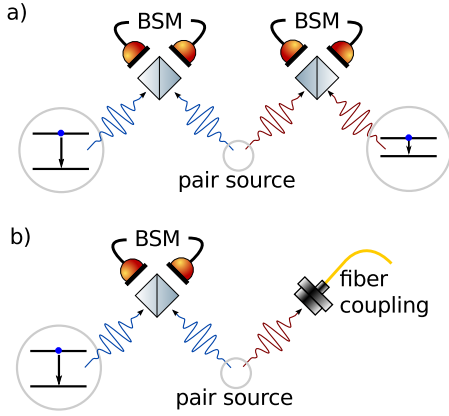


**Fig. 1** Scheme of entanglement distribution via a two-color entangled photon source. a) Two Bell-state measurements (BSM) on photons from two stationary qubit/flying qubit entangled systems and two photons from a two-color entangled photon source establish entanglement between two stationary qubits. b) Similarly, a single Bell-state measurement on a photon from a stationary qubit/flying qubit entangled system and one photon from a two-color entangled photon source establishes entanglement between the stationary qubit and a telecom photon.

additional dispersion, whereas this is not needed in a two-crystal Sagnac configuration.

Together with the pump, any two-color entangled photon source involves three fields of widely different wavelengths. This imposes strong constraints on dispersion compensation. In particular, a source for generating entanglement in quantum hybrid systems should be easy to align, intrinsically stable, and tunable in order to account for various transition frequencies. The Sagnac configuration requires a special three-color beam splitter and is very difficult to align [14]. The crossed-crystal configuration lacks the phase stability of the Sagnac configuration. Therefore it is desirable to use the simpler folded-sandwich configuration. In this paper we describe the realization of such a configuration. In contrast to previous work, we employ geometrical, i.e., wavelength independent, polarization manipulation.

Here, we target for a two-color entangled photon source at  $\lambda_s = 894.3 \text{ nm}$  and  $\lambda_i = 1313.1 \text{ nm}$ . These two wavelengths correspond to the Cs D1 line and the telecom O-band, respectively. The former has been chosen on the one hand as a convenient standard atomic transition. On the other hand it is also accessible with excitonic transitions in InGaAs quantum dots [15]. The source is thus applicable for quantum hybrid architectures [16,17] involving atomic species, semiconductor quantum dots or molecules as well as long distance transfer via optical fibers.

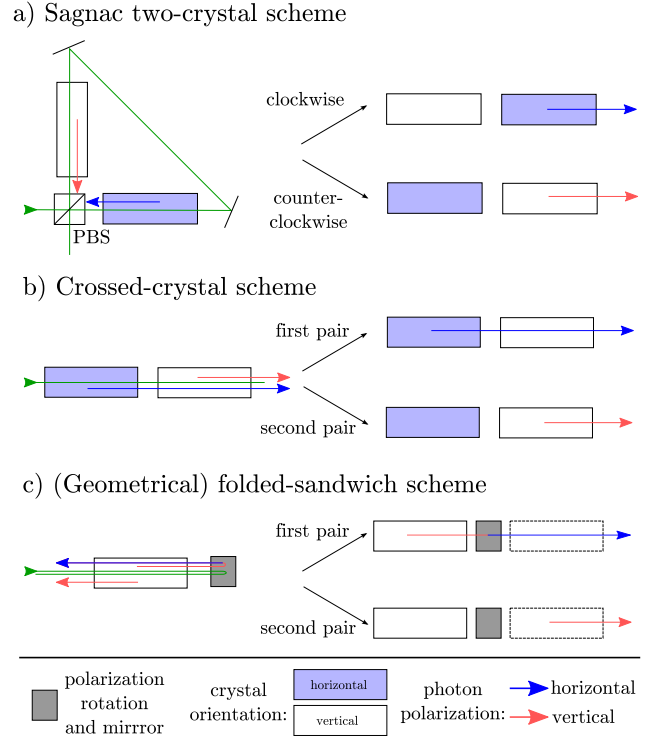


**Fig. 2** Different schemes of two-color collinear entangled photon pair sources using type-0 down-conversion. A horizontally (vertically) polarized pump photon in an appropriately, i.e., horizontal (vertical) crystal creates horizontally (vertically) polarized signal and idler photons. No photons are created when pump polarization and crystal orientation are orthogonal. a) The two possible paths in the two-crystal Sagnac configuration. In the clockwise and counter-clockwise path the photon pair is generated in the second crystal. In the (counter) clockwise path, the photon pair is generated vertically (horizontally) because the second crystal has horizontal (vertical) orientation. b) The two paths in the crossed-crystal configuration. The first photon pair (vertically polarized) is created in the first crystal and accumulates an extra phase while passing through the second crystal. The second photon pair is created in the last crystal, just as the counter-clockwise photon in the Sagnac configuration. c) Folded-sandwich configuration. The polarization rotation element and a mirror (both depicted as one gray box) rotate and reflect the first pair. This is equivalent to the first pair in the crossed-crystal scheme, only that instead of the crystal the light polarization is rotated. In the folded-sandwich configuration the second crystal is the mirrored first crystal. The (diagonal or unpolarized) pump beam is depicted in green.

## 2 Setup

The setup is shown in Fig. 3. It resembles a folded-sandwich, but the specifically tailored achromatic quarter-wave plate which is used in [14] is replaced by a wavelength independent Fresnel rhomb. The Fresnel rhomb yields a  $\lambda/4$  phase shift after two internal reflections. A diagonal polarized pump laser (532 nm cw) is focused into the non-linear crystal (length 40 mm, facet 4 mm  $\times$  1 mm, type-0 phase matching, grating period of 7

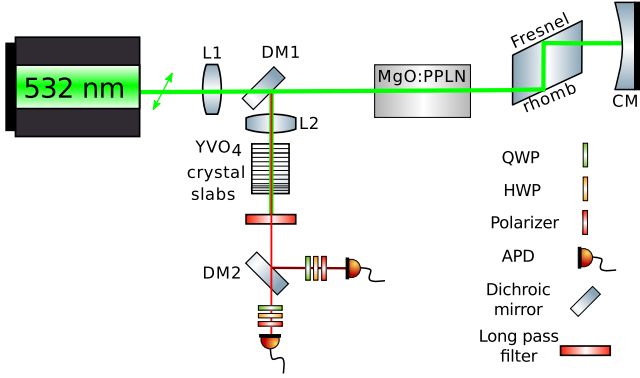


**Fig. 3** Setup based on one periodically poled lithium niobate crystal (ppLN) doped with approximately 5% magnesium oxide (MgO), of length  $L = 40$  mm. The crystal temperature is controlled via a crystal oven (not shown). The Fresnel rhomb acts as a geometrical quarter-wave plate. The concave mirror (CM) reflects the light back into the crystal. The focusing (L1) and collimation (L2) lenses adjust the beam width. The first dichroic mirror (DM1) separates pump and down-converted photons. The second dichroic mirror (DM2) separates signal and idler photons. The phase compensation crystal consists of several YVO<sub>4</sub> slabs to allow for dispersion control for a broad range of wavelengths. Both crystal ovens are omitted in this figure [18].

$\mu\text{m}$ , multiple gratings, HC Photonics Corp.). In this first pass, the vertical component of the diagonal pump beam may create a vertically polarized pair. This pair and the pump beam propagate through the Fresnel rhomb. The Fresnel rhomb is oriented at  $45^\circ$ , such that it acts on the vertically polarized photons as a quarter-wave plate. The vertical pair leaves the rhomb circularly polarized. The diagonal pump beam passes the Fresnel rhomb without modification. The concave mirror (CM) reflects the light back onto the Fresnel rhomb and into the crystal. The mirror is adjusted to reflect the light into the same spatial mode. On the way back the Fresnel rhomb rotates the circularly polarized pair into a horizontally polarized pair.

The diagonal pump beam and the horizontally polarized pair pass the non-linear crystal a second time. Again, the vertical part of the diagonal pump beam may create a vertically polarized pair. The pump power is chosen such that the probability for creating more than one pair per double-pass is low. The pump beam and the created photons are separated at the dichroic mirror (DM1). The photon pair is then collimated (L2) and directed onto a compensation crystal. Finally, signal and idler photons are separated at a dichroic mirror (DM2). In each of the separate arms, wave-plates and polarizers allow for measurement of different polarization states. Each arm is coupled to a single-mode fiber. The fibers can either be connected to a spectrograph

or to avalanche photo diodes (APDs) for spectral or coincidence measurements.

In order to generate an entangled state of the form

$$|\psi\rangle = \frac{1}{\sqrt{2}} (|VV\rangle + e^{i\phi}|HH\rangle). \quad (1)$$

it is required to compensate for the different dispersive characteristics accumulated by the first pair due to the extra pass through the rhomb and the non-linear crystal. Otherwise this accumulated which-crystal information would diminish the entanglement.

The extra phase  $\phi$  of the first pair  $|HH\rangle$  is given by

$$\phi(\lambda_s, \lambda_i, T) = \left( \frac{n_o(\lambda_s, T)}{\lambda_s} + \frac{n_o(\lambda_i, T)}{\lambda_i} \right) L_{\text{crystal}} \quad (2)$$

$$+ \left( \frac{n_r(\lambda_s)}{\lambda_s} + \frac{n_r(\lambda_i)}{\lambda_i} \right) 2 L_{\text{rhomb}}, \quad (3)$$

where  $n_r$  is the refractive index of the Fresnel rhomb (BK7 glass of length  $L_{\text{rhomb}}$ ) and  $n_o$  is the refractive index of the ordinary (horizontal) non-linear crystal axis of length  $L_{\text{crystal}}$ . The refractive index of the non-linear crystal depends on the crystal temperature  $T$  and the wavelengths of the down-converted signal and idler photons  $\lambda_{s/i}$ .

In our experiment, we chose undoped YVO<sub>4</sub> as a birefringent compensation crystal. A crystal of length  $\tilde{L}$  adds a phase of

$$\tilde{\phi}(\lambda_s, \lambda_i, T) = \left( \frac{\tilde{n}_o(\lambda_s, T)}{\lambda_s} + \frac{\tilde{n}_o(\lambda_i, T)}{\lambda_i} - \frac{\tilde{n}_e(\lambda_s, T)}{\lambda_s} - \frac{\tilde{n}_e(\lambda_i, T)}{\lambda_i} \right) \tilde{L},$$

where  $\tilde{n}_{o/e}$  is the refractive index of the ordinary and extra-ordinary axis of YVO<sub>4</sub>.

The flat phase condition for optimum compensation with the two different photon wavelengths  $\lambda_s$  and  $\lambda_i$  reads:

$$\frac{d}{d\lambda} (\phi + \tilde{\phi}) \Big|_{\lambda_{s,i}} = 0. \quad (4)$$

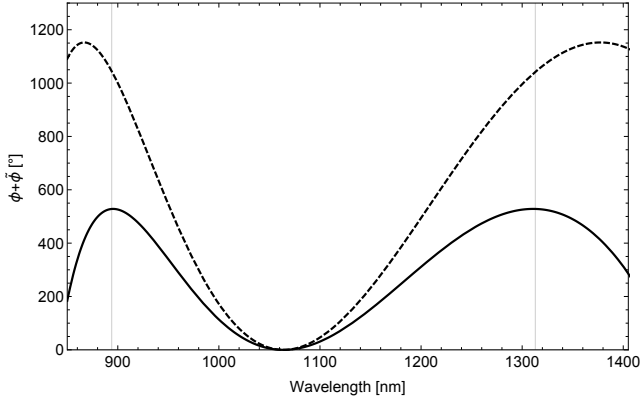
There are different values for the birefringent properties of YVO<sub>4</sub> in the literature. Table 1 lists the refractive index difference of the ordinary and extraordinary axis of YVO<sub>4</sub> and the calculated length of a compensation crystal for the wavelengths  $\lambda_s = 894.3$  nm and  $\lambda_i = 1313.1$  nm for different sources.

Figure 4 shows the calculated phase  $\phi + \tilde{\phi}$  as a function of the wavelength for two different lengths of the compensation crystal. The two target wavelengths  $\lambda_s = 894.3$  nm and  $\lambda_i = 1313.1$  nm are plotted as vertical lines.

For  $\pm 1$  mm crystal length, the two flat phase positions vary by  $\pm 50$  nm. Thus with adding or removing

**Table 1** Reported refractive index difference  $\Delta n = n_e - n_o$  of the ordinary and extraordinary axis of  $\text{YVO}_4$  from different sources and the calculated corresponding length of compensation crystal for  $\lambda_s = 894.3 \text{ nm}$  and  $\lambda_i = 1313.1 \text{ nm}$ .

Source	$\Delta n_s$	$\Delta n_i$	$L \text{ [mm]}$
Manufacturer (Foctek) [19]	0.211014	0.205272	138.7
Zelmon, et al. [20]	0.211408	0.205449	154.0
Sato, et al. [21]	0.213228	0.207146	172.0
Handbook of Optics [22]	0.209959	0.204679	178.8



**Fig. 4** Calculated phase  $\phi + \tilde{\phi}$  as a function of the wavelength for two different lengths of the compensation crystal (constant offset subtracted). A flat phase is obtained for  $\tilde{L} = 154 \text{ mm}$  (—) for the two target wavelengths  $\lambda_s = 894.3 \text{ nm}$  and  $\lambda_i = 1313.1 \text{ nm}$  (vertical lines). The plateaus of the flat phases are shifted considerably for  $\tilde{L} = 153 \text{ mm}$  (---).

additional few mm slabs of  $\text{YVO}_4$  the total compensation can be tuned by several hundred nanometers.

Finally, Fig. 5 demonstrates the tuning capability of our source. The crystal oven of the non-linear crystal can be heated up to  $160^\circ\text{C}$ . The measured tuning range of the signal photon wavelength for the chosen  $7 \mu\text{m}$  grating extends from  $870 \text{ nm}$  to  $1100 \text{ nm}$ , this is roughly  $230 \text{ nm}$ . The corresponding idler wavelength spans from  $1124 \text{ nm}$  to  $1345 \text{ nm}$  (not shown). The measurement was performed without compensation crystal.

### 3 Determining the Optimal Crystal Length

The wave-plates in each arm (after DM2 in Fig. 3) can be rotated such that photon coincidences in different bases can be measured. Both polarizers are fixed to horizontal polarization, such that in each arm the basis  $|H\rangle$  is measured for a half-wave plate position of  $\Theta_{\text{HWP}} = 0$ . Rotating the half-wave plate to  $\Theta_{\text{HWP}} = \pm 22.5^\circ$  the diagonal  $|D\rangle$  and anti-diagonal  $|A\rangle$  basis is measured, respectively. Adding a quarter-wave plate the left  $|L\rangle$  and right  $|R\rangle$  basis can be measured. Each arm can be set to an individual polarization. For example, setting both arms to left-circularly polarization is denoted  $|L\rangle_{\text{signal}}|L\rangle_{\text{idler}} = |LL\rangle$  in the following.

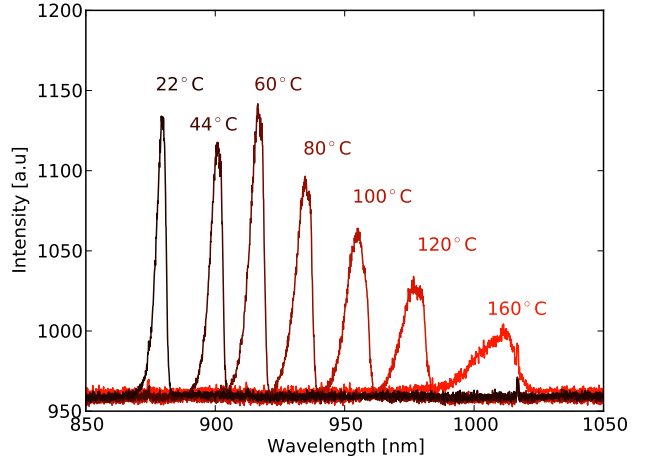


**Fig. 5** Spectra of signal photons for different temperatures of the non-linear crystal. The decreasing intensities with higher temperatures are due to decreasing sensitivity of the spectrometer CCD camera. At  $1064 \text{ nm}$  the signal and idler photons are degenerate.

The procedure to find the right compensation crystal relies on measuring polarization-sensitive coincidence counts as a function of the orientation of the half-wave plate  $\Theta_{\text{HWP}}$  in one arm. Fig. 6 shows such measurements in different bases combinations. The measured curve can be fitted to a sine function and the visibility can be derived (see next Section for details). Then, thin slabs of  $\text{YVO}_4$  are added, until the visibility cannot be enhanced further. In this way an optimum total length of the compensation crystal can be found.

Unfortunately, tuning by adding thin slabs of additional compensation crystals does not provide sufficient accuracy. Therefore a fine tuning of the phase between  $0$  and  $\pi$  to generate a specific Bell-state is necessary.

In order to do this we changed the temperature of a  $30 \text{ mm}$  compensation crystal slab. Figure 7 shows the measured coincidence counts between signal and idler photons in the  $|AA\rangle$  basis as a function of the temperature of the compensation crystal. We find a phase shift of  $\pi$ , i.e., between two different Bell-states, for  $\sim 2.4^\circ\text{C}$  temperature difference.

For the wavelengths  $\lambda_s = 894.3 \text{ nm}$  and  $\lambda_i = 1313.1 \text{ nm}$  we find a optimal total crystal length of  $L = 153 \text{ mm}$ . The total length was composed of 7 slabs  $\text{YVO}_4$  of  $2 \text{ cm}$  length and one slab of  $1 \text{ cm}$ ,  $2 \text{ mm}$  and  $1 \text{ mm}$  length. The total length is close to some of the reported data on the refractive index of  $\text{YVO}_4$  in literature [20], even though they investigated  $0.5\%$  Nd-doped  $\text{YVO}_4$ . However, it deviates from the value reported by other studies [21], as well as from the manufacturer specification (Foctek Inc.) [19].

With the experimentally determined crystal parameters, it is in principle straightforward to estimate the

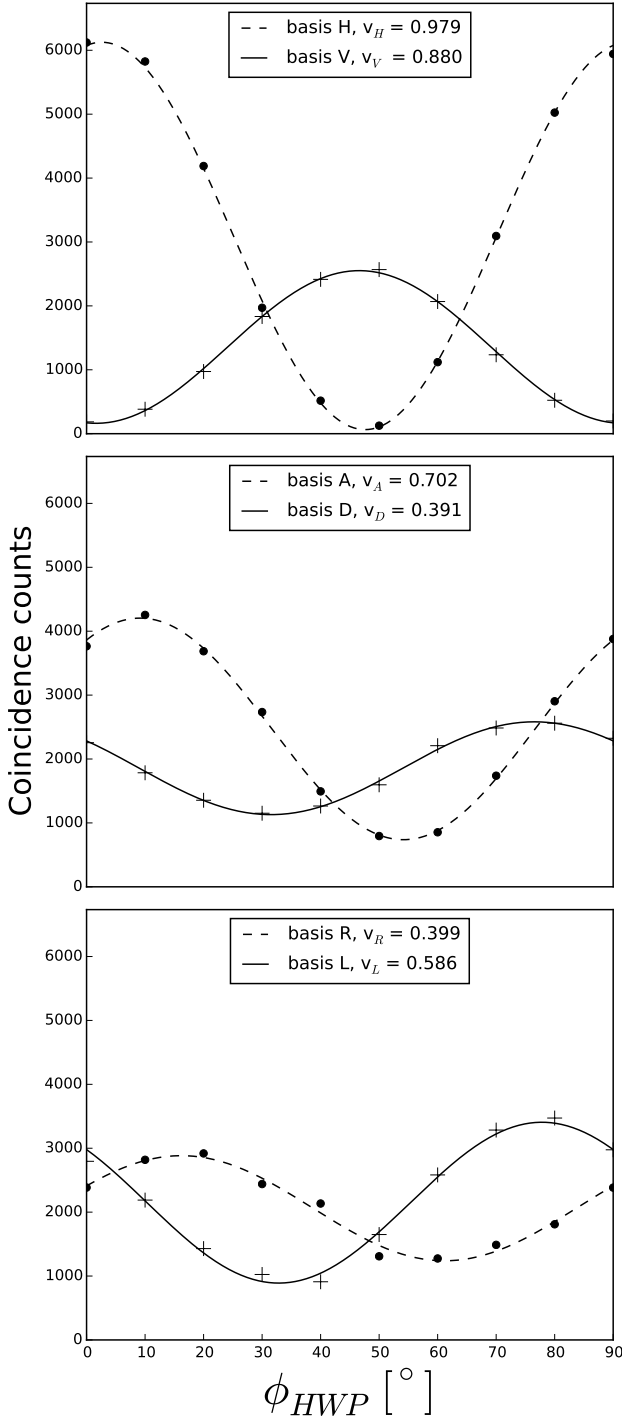


**Fig. 6** Measured coincidence counts as a function of the orientation of the half-wave plate in different basis combinations. The dashed and solid lines are fits to sine-functions. The resulting visibilities  $v_i$  from Eq. (15) are indicated.

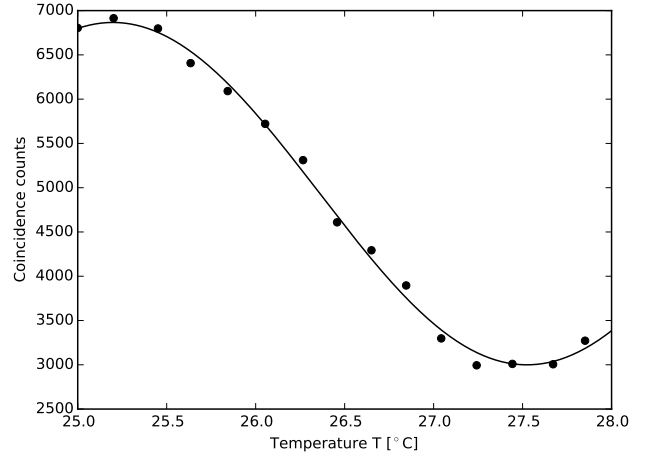


**Fig. 7** Measured coincidence counts in the  $|AA\rangle$  basis (both polarizers anti-diagonal) as a function of the temperature of a 30 mm compensation crystal slab. The total crystal length is 153 mm.

compensation crystal length also for other pairs of wavelengths. Additional crystal slabs can be added or removed allowing for a wide tuning range.

#### 4 Verifying Entanglement

To quantify the degree of entanglement for optimized conditions, we measured the  $|\phi^+\rangle$  Bell-state fidelity  $F_{\phi^+}$  of the created state  $\rho$ ,

$$F_{\phi^+} = \langle \phi^+ | \rho | \phi^+ \rangle. \quad (5)$$

A fidelity  $F_{\phi^+} > \frac{1}{2}$  indicates entanglement [23]. In order to relate the fidelity to the coincidence probabilities we use the two-photon polarization basis states  $|u_1\rangle = |HH\rangle$ ,  $|u_2\rangle = |HV\rangle$ ,  $|u_3\rangle = |VH\rangle$ ,  $|u_4\rangle = |VV\rangle$ . After expanding  $\rho$  in this basis and using

$$|\phi^+\rangle = \frac{1}{\sqrt{2}} (|u_1\rangle + |u_4\rangle), \quad (6)$$

we get

$$\begin{aligned} F_{\phi^+} &= \sum_{k,l=1}^4 \rho_{kl} \langle \phi^+ | u_k \rangle \langle u_l | \phi^+ \rangle \\ &= \frac{1}{2} (\rho_{11} + \rho_{14} + \rho_{41} + \rho_{44}), \end{aligned} \quad (7)$$

where  $\rho_{kl} = \langle u_k | \rho | u_l \rangle$ . The diagonal elements  $\rho_{11}$  and  $\rho_{44}$  are the probabilities  $P_H$  and  $P_V$  of finding a photon pair in the states  $|HH\rangle$  and  $|VV\rangle$ , respectively. The off-diagonal elements can be expressed with the help of

the diagonal and circular basis,

$$P_D + P_A = \langle DD|\rho|DD\rangle + \langle AA|\rho|AA\rangle \\ = \frac{1}{2}(1 + \rho_{14} + \rho_{41} + \rho_{23} + \rho_{32}), \quad (8)$$

$$P_R + P_L = \frac{1}{2}(1 - \rho_{14} - \rho_{41} + \rho_{23} + \rho_{32}) \quad (9)$$

and thus

$$P_D + P_A - (P_R + P_L) = \rho_{14} + \rho_{41}. \quad (10)$$

We therefore obtain the fidelity as a function of the probabilities in the three different bases,

$$F_{\phi^+} = \frac{1}{2}[P_D + P_A - (P_R + P_L) + P_H + P_V]. \quad (11)$$

These probabilities can be measured as they are connected to the coincidence count rates  $N$ ,

$$P_i = \frac{N_{ii}}{N_{ii} + N_{ij} + N_{jj} + N_{ji}} = \frac{N_{ii}}{N_{tot}}, \quad (12)$$

where  $i$  refers to the one photon polarization state orthogonal to  $j$ , that is  $i/j = H/V, D/A$ , or  $L/R$ . After introducing

$$V_{ij} = \frac{N_{ii} + N_{jj} - (N_{ij} + N_{ji})}{N_{ii} + N_{jj} + N_{ij} + N_{ji}} = \frac{2(N_{ii} + N_{jj})}{N_{tot}} - 1 \quad (13)$$

Eq. ((11)) yields the alternative representation [14]

$$F_{\phi^+} = \frac{1}{4}(1 + V_{HV} + V_{DA} - V_{LR}). \quad (14)$$

To determine the fidelity, we measured the visibilities

$$v_i = \frac{N_{ii} - N_{ij}}{N_{ii} + N_{ij}} = \frac{A_i}{C_i} \quad (15)$$

in the 3 different bases, as shown in Fig. 6. In the measurement the basis in one arm is fixed, while the basis in the other arm is rotated between  $i$ , and its orthogonal counter part  $j$ . The visibilities are then fitted with a sine function  $A_i \sin(4\phi_{HWP} + \text{const.}) + C_i$ . Since  $C_i = (N_{ii} + N_{ij})/2$  and  $A_i = (N_{ii} - N_{ij})/2$ , we have

$$V_{ij} = \frac{A_i + A_j}{C_i + C_j}. \quad (16)$$

With this we find a fidelity of  $F_{\phi^+} = 0.753 \pm 0.021$  for our source at a photon pair generation rate of 5.8 Mcps/mW and spectral linewidths of 560 GHz, which corresponds to 1.5 nm and 3.3 nm at  $\lambda_s = 894.3$  nm and  $\lambda_i = 1313.1$  nm, respectively.

The limited visibility can be explained by temperature fluctuations of the compensation crystals. The total length of the compensation crystal is  $L = 153$  mm, but

only a small fraction (3 cm) of the crystal is temperature stabilized inside the crystal oven. Small changes in temperature modify the optical path-lengths of extraordinarily and ordinarily polarized photons and lead to a fluctuating phase. For our configuration the temperature fluctuations at the compensation crystals of  $\pm 1$  K are the strongest factor that reduces the fidelity (see also [14]). With an improved temperature stabilization and a thermally isolated housing of the compensation crystals fidelities above 95% should be possible [14].

## 5 Conclusion

We demonstrated a novel folded-sandwich scheme for the generation of two-color entangled photons which uses a Fresnel rhomb as a geometrical quarter-wave plate. By this, all optical components are more easily adapted to wide combinations of wavelengths. For example, no three-color beam splitters as in a Sagnac configuration are required. Adjusting the compensation crystal length offers a tuning capability over more than 100 nm. Our source is a viable tool to provide highly non-degenerate entangled photons for quantum hybrid architectures, in particular when solid-state emitters with an a priori unpredictable transition frequency are involved.

## 6 Acknowledgements

This work was funded by BMBF (Q.com-H). Funding by DFG through SFB 787 is acknowledged by O.D. O.D. likes to thank Sven Ramelow, Fabian Steinlechner and Amir Moqanaki for their hospitality during his stay in Vienna and their continuous input and support on the experimental design. This work was also supported by project EMPIR 14IND05 MIQC2 (the EMPIR initiative is co-funded by the European Union's Horizon 2020 research and innovation programme and the EMPIR Participating States).

## References

1. H.J. Briegel, W. Dür, J.I. Cirac, P. Zoller, Phys. Rev. Lett. **81**(26), 5932 (1998). DOI 10.1103/PhysRevLett.81.5932. URL <http://link.aps.org/doi/10.1103/PhysRevLett.81.5932>
2. J. Volz, M. Weber, D. Schlenk, W. Rosenfeld, J. Vrana, K. Saucke, C. Kurtsiefer, H. Weinfurter, Phys. Rev. Lett. **96**(3), 030404 (2006). DOI 10.1103/PhysRevLett.96.030404. URL <http://link.aps.org/doi/10.1103/PhysRevLett.96.030404>
3. B.B. Blinov, D.L. Moehring, L.M. Duan, C. Monroe, Nature **428**(6979), 153 (2004). DOI 10.1038/nature02377. URL <http://www.nature.com/nature/journal/v428/n6979/full/nature02377.html>

4. W.B. Gao, P. Fallahi, E. Togan, J. Miguel-Sanchez, a. Imamoglu, *Nature* **491**(7424), 426 (2012). DOI 10.1038/nature11573. URL <http://www.nature.com/doi/10.1038/nature11573>
5. E. Togan, Y. Chu, A.S. Trifonov, L. Jiang, J. Maze, L. Childress, M.V.G. Dutt, A.S. Sørensen, P.R. Hemmer, A.S. Zibrov, M.D. Lukin, *Nature* **466**(7307), 730 (2010). DOI 10.1038/nature09256. URL <http://www.nature.com/nature/journal/v466/n7307/full/nature09256.html>
6. A. Wallraff, D.I. Schuster, A. Blais, L. Frunzio, R.S. Huang, J. Majer, S. Kumar, S.M. Girvin, R.J. Schoelkopf, *Nature* **431**(7005), 162 (2004). DOI 10.1038/nature02851. URL <http://www.nature.com/nature/journal/v431/n7005/full/nature02851.html>
7. J. Hofmann, M. Krug, N. Ortegel, L. Gérard, M. Weber, W. Rosenfeld, H. Weinfurter, *Science* **337**(6090), 72 (2012). DOI 10.1126/science.1221856. URL <http://www.sciencemag.org/content/337/6090/72>
8. H. Bernien, B. Hensen, W. Pfaff, G. Koolstra, M.S. Blok, L. Robledo, T.H. Taminiau, M. Markham, D.J. Twitchen, L. Childress, R. Hanson, *Nature* **497**(7447), 86 (2013). DOI 10.1038/nature12016. URL <http://www.nature.com/nature/journal/v497/n7447/abs/nature12016.html>
9. P.G. Kwiat, K. Mattle, H. Weinfurter, A. Zeilinger, A.V. Sergienko, Y. Shih, *Phys. Rev. Lett.* **75**(24), 4337 (1995). DOI 10.1103/PhysRevLett.75.4337. URL <http://link.aps.org/doi/10.1103/PhysRevLett.75.4337>
10. M. Pelton, P. Marsden, D. Ljunggren, M. Tengner, A. Karlsson, A. Fragemann, C. Canalias, F. Laurell, *Optics Express* **12**(15), 3573 (2004). DOI 10.1364/OPEX.12.003573. URL <http://www.opticsexpress.org/abstract.cfm?URI=OPEX-12-15-3573>
11. M. Hentschel, H. Hübel, A. Poppe, A. Zeilinger, *Optics express* **17**(25), 23153 (2009). URL <http://www.opticsinfobase.org/abstract.cfm?uri=oe-17-25-23153>
12. T.E. Stuart, J.A. Slater, F. Bussières, W. Tittel, *Physical Review A* **88**(1) (2013). DOI 10.1103/PhysRevA.88.012301. URL <http://link.aps.org/doi/10.1103/PhysRevA.88.012301>
13. P. Trojek, H. Weinfurter, *Applied Physics Letters* **92**(21), 211103 (2008). DOI 10.1063/1.2924280. URL <http://scitation.aip.org/content/aip/journal/apl/92/21/10.1063/1.2924280>
14. F. Steinlechner, S. Ramelow, M. Jofre, M. Gilaberte, T. Jennewein, M.W. Mitchell, V. Pruneri, J.P. Torres, *Optics Express* **21**(10), 11943 (2013). DOI 10.1364/OE.21.011943. URL <http://www.opticsinfobase.org/abstract.cfm?URI=oe-21-10-11943>
15. F. Ding, R. Singh, J.D. Plumhof, T. Zander, V. Kápek, Y.H. Chen, M. Benyoucef, V. Zwiller, K. Dörr, G. Bester, A. Rastelli, O.G. Schmidt, *Phys. Rev. Lett.* **104**(6), 067405 (2010). DOI 10.1103/PhysRevLett.104.067405. URL <http://link.aps.org/doi/10.1103/PhysRevLett.104.067405>
16. N. Akopian, L. Wang, A. Rastelli, O.G. Schmidt, V. Zwiller, *Nat Photon* **5**(4), 230 (2011). DOI 10.1038/nphoton.2011.16. URL <http://www.nature.com/nphoton/journal/v5/n4/full/nphoton.2011.16.html>
17. P. Siyushev, G. Stein, J. Wrachtrup, I. Gerhardt, *Nature* **509**(7498), 66 (2014). DOI 10.1038/nature13191. URL <http://www.nature.com/nature/journal/v509/n7498/full/nature13191.html>
18. Alexander Franzen. ComponentLibrary: a free vector graphics library for optics. Licensed under a Creative Commons Attribution-NonCommercial 3.0 Unported License. URL <http://www.gwoptics.org/ComponentLibrary/>
19. Focetek Photonics, Inc. YVO4. URL <http://www.focetek.net/products/YVO4.htm>
20. D.E. Zelmon, J.M. Northridge, D. Perlov, *Appl. Opt.* **49**(4), 644 (2010). DOI 10.1364/AO.49.000644. URL <http://ao.osa.org/abstract.cfm?URI=ao-49-4-644>
21. Y. Sato, T. Taira, *Opt. Mater. Express* **4**(5), 876 (2014). DOI 10.1364/OME.4.000876. URL <http://www.opticsinfobase.org/ome/abstract.cfm?URI=ome-4-5-876>
22. M. Bass, C. DeCusatis, J. Enoch, V. Lakshminarayanan, G. Li, C. MacDonald, V. Mahajan, E.V. Stryland, *Handbook of Optics, Third Edition Volume IV: Optical Properties of Materials, Nonlinear Optics, Quantum Optics (set): Optical Properties of Materials, Nonlinear Optics, Quantum Optics (set)* (McGraw Hill Professional, 2009)
23. A.G. White, A. Gilchrist, G.J. Pryde, J.L. O'Brien, M.J. Bremner, N.K. Langford, *JOSA B* **24**(2), 172 (2007). URL <http://www.opticsinfobase.org/abstract.cfm?uri=josab-24-2-172>